J. Fluid Mech. (2001), *vol.* 429, *pp.* 239–254. Printed in the United Kingdom

Wake formation around islands in oscillatory laminar shallow-water flows. Part 2. Three-dimensional boundary-layer modelling

By PETER K. STANSBY AND PETER M. LLOYD†

Department of Civil and Construction Engineering, UMIST, Manchester M60 1QD, UK

(Received 6 December 1999 and in revised form 4 August 2000)

A three-dimensional numerical model for shallow-water flow with the assumption of hydrostatic pressure has been applied to oscillatory laminar flow around a conical island of small side slope (8°). The model is (mainly) second-order accurate in space and time with advection in conservation form. This form of model is effectively a boundary-layer solution with imposed depth-integrated continuity. To reproduce experimental conditions particular care was required for boundary conditions to account for seiching in the flume. The model predicted the wide range of wake structures observed experimentally and described in Part 1 (Lloyd, Stansby & Chen 2001), from symmetric with weak vortex pairing to complex vortex shedding.

1. Introduction

Since the early work of Leendertse (1967) there have been numerous contributions to the numerical modelling of shallow-water flows. Early models were in depth-averaged form due to computational limitations and these are indeed still popular. The vertical velocity variation has of course to be assumed which may not be a severe limitation if the boundary layer is fully developed through the water depth; in particular the bed friction coefficient has to be specified. However for the problem of this paper it has been mentioned in Part 1 (Lloyd, Stansby & Chen 2001) that the boundary-layer thickness is generally less than the water depth and it is thus impossible to specify the bed friction without numerical modelling of the boundary layer. Here we adopt a three-dimensional form of the shallow-water equations while still making the assumption of hydrostatic pressure. This enables the boundary-layer development to be computed directly (without explicit reference to a bed friction coefficient) but does not allow realistic representation of separation in a vertical plane which depends on the complete pressure (hydrostatic plus non-hydrostatic). The hydrostatic pressure assumption essentially requires bed slopes to be small. It also requires water surface slopes to be small although this is generally not a limitation for subcritical tidal flow problems. Non-hydrostatic pressure has been incorporated within a shallow-water numerical solution (Stansby & Zhou 1998; Zhou & Stansby 1999) but this is computationally very time-consuming and here we restrict our modelling to the case of the island with gently sloping sides. It is of considerable interest to know whether such a relatively efficient formulation will predict the complex wake formations due to a gently sloping obstacle at low subcritical Froude numbers.

† Present address: Tessella Support Services plc, Robert Gordon House, Cavendish Avenue, Birchwood Park, Warrington WA3 6FT, UK.

There are numerous other modelling decisions to be made. Fixed Cartesian meshes have been used for shallow-water flows in the past but they cannot allow an accurate resolution of the bed and water surface (both are obviously vital considerations). Here we adopt a mesh automatically fitted to the bed and water surface, the σ-coordinate system (Phillips 1957). The mesh is fixed in the horizontal plane although the edge of the flow domain, the wet/dry boundary, is moving. However the velocities (more importantly the horizontal velocity gradients) in such regions are small and the movement of the wet/dry boundary can be accommodated by simple physical arguments. (This is in contrast to, for example, aerodynamic flows around bodies where velocity gradients are very high at a solid boundary and high resolution is vital.) The numerical scheme used here is developed from Stansby (1997).

Spatial and temporal discretization are further considerations. Finite-difference and finite-element spatial discretization can be made of arbitrary high order while the finite-volume method is generally limited to second-order accuracy. However the finite-volume scheme guarantees global conservation of important quantities, mass and momentum flux in this problem, and second-order accuracy is generally adequate (in fact finite difference and element schemes rarely use greater order of accuracy). Upwind difference schemes for advection are also generally only second-order accurate (notably the popular QUICK scheme). Temporal discretization has arguably received less attention. Many schemes have been explicit and only first-order accurate. Implicit time-stepping is clearly desirable for stability and has become more popular with increasing computer power and more efficient equation solvers (principally multigrid and conjugate gradient methods). An effective (depth-averaged) scheme with first-order semi-implicit time-stepping on a staggered finite-difference mesh (effectively a finite-volume method) is due to Casulli (1989). It has since been shown by Casulli & Cattani (1994) that such a scheme has significant wave damping and numerical diffusion for linearized one-dimensional shallow-water equations but with second-order Crank–Nicolson ($\theta = 1/2$) time-stepping this becomes negligible. For two-dimensional vertical plane solutions of the shallow-water equations with non-hydrostatic pressure for short-crested wave propagation, Zhou & Stansby (1999) demonstrate lack of wave damping and numerical diffusion in a more general formulation. This time-stepping approach has been maintained for this three-dimensional formulation with the hydrostatic pressure assumption. Advection accuracy is known to be vital for realistic prediction of recirculating flows and here the QUICK scheme is used to give second-order spatial accuracy. The advection scheme in conservation form is also effective for wave capturing. These terms are treated explicitly and to maintain second-order temporal accuracy the Adams–Bashforth scheme is incorporated. Horizontal diffusion is also treated explicitly and the second-order Adams–Bashforth scheme is used here also. However vertical diffusion is treated semi-implicitly only to first-order accuracy to enhance stability and hence produce an overall scheme which is robust. This latter approach has now been widely applied to one-dimensional boundary-layer problems (including turbulence modelling) and has been found to give accurate solutions (Stansby 1997; Letherman *et al.* 2000).

The application here is to laminar flow but complex wake flows have been observed experimentally to be sensitive to the stability parameter, $S = c_f D/h$, Keulegan–Carpenter number, $KC = U_o T/D$, and D/h, where c_f is friction coefficient, U_o is velocity amplitude (both in the ambient flow), T is oscillation period, D is diameter at mid-depth and h is depth. It is the intention here to determine how well a three-dimensional boundary-layer formulation in a shallow-water context will predict the experimental results.

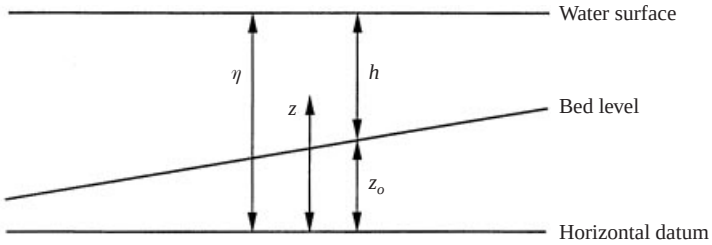

FIGURE 1. Definition sketch.

2. Mathematical formulation

The continuity and Navier–Stokes equations in Cartesian form are converted to σ-coordinates to automatically fit the bed and the moving water surface, enabling high mesh resolution to be easily produced as may be required in those regions.

The σ-coordinate is defined as

$$\sigma = \frac{z-\eta}{h} \tag{1}$$

where η is surface elevation, h is water depth and z is the vertical coordinate, as shown in figure 1.

The grid is generally fixed in the horizontal (x, y)-plane but grid movement in the vertical direction should be accounted for as in an ALE (arbitrary Lagrangian–Eulerian) formulation. Within a σ-coordinate context this is referred to as ALES (Zhou & Stansby 1999). If the velocities in Cartesian coordinates are u, v, w in the x-, y-, z-directions, in the σ-coordinate system $u_\sigma = u$, $v_\sigma = v$ and $w_\sigma = \omega/h$ (defined below) and the σ subscript is dropped hereafter for u and v. With the hydrostatic pressure assumption for pressure p, $\partial p/\partial\sigma = -\rho g h$, $\partial p/\partial x = \rho g\, \partial\eta/\partial x$ and $\partial p/\partial y = \rho g\, \partial\eta/\partial y$ where ρ is water density and g is gravitational acceleration. The shallow-water equations in conservation form may be written:

for local continuity

$$\frac{\partial\eta}{\partial t} + \frac{\partial(hu)}{\partial x} + \frac{\partial(hv)}{\partial y} + \frac{\partial\omega}{\partial\sigma} = 0, \tag{2}$$

for x-momentum

$$\frac{\partial(hu)}{\partial t} + \frac{\partial(hu^2)}{\partial x} + \frac{\partial(huv)}{\partial y} + \frac{\partial(\omega u)}{\partial\sigma} - w_g\frac{\partial u}{\partial\sigma} = -gh\frac{\partial\eta}{\partial x} + \frac{\partial}{\partial\sigma}\left(\frac{\nu}{h}\frac{\partial u}{\partial\sigma}\right) + \frac{\partial}{\partial x}\left(\nu\frac{\partial(hu)}{\partial x}\right) + \frac{\partial}{\partial y}\left(\nu\frac{\partial(hu)}{\partial y}\right), \tag{3}$$

for y-momentum

$$\frac{\partial(hv)}{\partial t} + \frac{\partial(huv)}{\partial x} + \frac{\partial(hv^2)}{\partial y} + \frac{\partial(\omega v)}{\partial\sigma} - w_g\frac{\partial v}{\partial\sigma} = -gh\frac{\partial\eta}{\partial y} + \frac{\partial}{\partial\sigma}\left(\frac{\nu}{h}\frac{\partial v}{\partial\sigma}\right) + \frac{\partial}{\partial x}\left(\nu\frac{\partial(hv)}{\partial x}\right) + \frac{\partial}{\partial y}\left(\nu\frac{\partial(hv)}{\partial y}\right), \tag{4}$$

where w_g is vertical grid velocity, ν is kinematic viscosity and

$$\omega = h\frac{\mathrm{d}\sigma}{\mathrm{d}t} = w - u\left(\sigma\frac{\partial h}{\partial x} + \frac{\partial\eta}{\partial x}\right) - v\left(\sigma\frac{\partial h}{\partial y} + \frac{\partial\eta}{\partial y}\right) - \left(\sigma\frac{\partial h}{\partial t} + \frac{\partial\eta}{\partial t}\right); \tag{5}$$

$\omega = 0$ when $\sigma = 0$ or -1, corresponding to the water surface and the bed respectively.

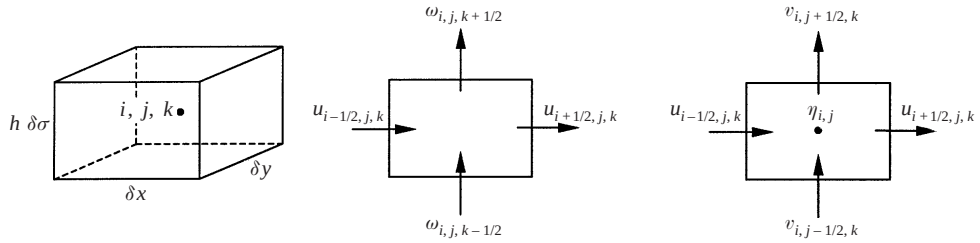

Cell centred on i, j, k Vertical (x, σ) plane Horizontal (x, y) plane

FIGURE 2. Staggered mesh system.

The depth-integrated continuity equation is given by

$$\frac{\partial \eta}{\partial t} + \frac{\partial}{\partial x}\int_{-1}^{0} hu \, \mathrm{d}\sigma + \frac{\partial}{\partial y}\int_{-1}^{0} hv \, \mathrm{d}\sigma = 0. \tag{6}$$

In the numerical scheme we compress the σ-mesh near the bed using a parabolic transformation (similar to that in Stansby 1997) with mesh spacing at the bed generally made equal to the diffusion length in one time step $\sqrt{2\nu\delta t}$, as widely used in many boundary-layer computations, where ν is kinematic viscosity and δt is time step. In the discretization below we also use a uniformly spaced σ'-mesh, $0 \leqslant \sigma' \leqslant 1$.

3. Discretization and solution

It is not possible generally to use the flux terms hu, hv as variables since u, v appear in isolation in the vertical advection and diffusion terms, the latter being most significant for these flows, although hu, hv are used for the horizontal advection terms. The solution method for each time step is essentially to substitute horizontal velocities obtained from the momentum equations into the depth-integrated continuity equation for each horizontal mesh point, giving a five-diagonal equation set for surface elevation η which is then solved by a conjugate gradient method. The flow is thus defined and horizontal velocities are retrieved. Vertical velocity is obtained from local continuity; this is a small correction to $\omega = 0$ within the limitation of negligible vertical acceleration due to the hydrostatic pressure assumption. To avoid checkerboard oscillations we use the conventional staggered mesh system shown in figure 2 with cells numbered centrally as $i, j, k (i = 1, I; j = 1, J; k = 1, K$ with $k = 1$ for the bed cell and $k = K$ for the surface cell). The horizontal cell widths are δx and δy.

The momentum equations within a finite-volume formulation with Crank–Nicolson time-stepping as mentioned above take the following discretized form with the explicit terms lumped into the operator F:

$$u^{n+1}_{i+1/2,j,k} = \mathrm{F}u^{n}_{i+1/2,j,k} - \theta g \frac{\delta t}{\delta x}(\eta^{n+1}_{i+1,j} - \eta^{n+1}_{i,j}) - (1-\theta) g \frac{\delta t}{\delta x}(\eta^{n}_{i+1,j} - \eta^{n}_{i,j})$$
$$+ \nu \delta t \frac{\left(\dfrac{\partial \sigma'}{\partial \sigma}\right)_{k+1/2}(u^{n+1}_{i+1/2,j,k+1} - u^{n+1}_{i+1/2,j,k}) - \left(\dfrac{\partial \sigma'}{\partial \sigma}\right)_{k-1/2}(u^{n+1}_{i+1/2,j,k} - u^{n+1}_{i+1/2,j,k-1})}{(\delta \sigma' h^{n}_{i+1/2,j})^2 \left(\dfrac{\partial \sigma}{\partial \sigma'}\right)_{k}}, \tag{7}$$

$$v^{n+1}_{i,j+1/2,k} = \mathrm{F}v^{n}_{i,j+1/2,k} - \theta g\frac{\delta t}{\delta y}(\eta^{n+1}_{i,j+1} - \eta^{n+1}_{i,j}) - (1-\theta)g\frac{\delta t}{\delta y}(\eta^{n}_{i,j+1} - \eta^{n}_{i,j})$$
$$+\nu\delta t\frac{\left(\dfrac{\partial\sigma'}{\partial\sigma}\right)_{k+1/2}(v^{n+1}_{i,j+1/2,k+1} - v^{n+1}_{i,j+1/2,k}) - \left(\dfrac{\partial\sigma'}{\partial\sigma}\right)_{k-1/2}(v^{n+1}_{i,j+1/2,k} - v^{n+1}_{i,j+1/2,k-1})}{(\delta\sigma' h^{n}_{i,j+1/2})^2\left(\dfrac{\partial\sigma}{\partial\sigma'}\right)_k}, \tag{8}$$

where n denotes time level, θ is the Crank–Nicolson variable, δt is time step, $\delta\sigma' = 1/K$. In compact matrix-vector form

$$A^{n}_{i+1/2,j}U^{n+1}_{i+1/2,j} = G^{n}_{i+1/2,j} - \theta g\frac{\delta t}{\delta x}(\eta^{n+1}_{i+1,j} - \eta^{n+1}_{i,j})h^{n}_{i+1/2,j}\Delta\sigma, \tag{9}$$

$$A^{n}_{i,j+1/2}V^{n+1}_{i,j+1/2} = G^{n}_{i,j+1/2} - \theta g\frac{\delta t}{\delta y}(\eta^{n+1}_{i,j+1} - \eta^{n+1}_{i,j})h^{n}_{i,j+1/2}\Delta\sigma, \tag{10}$$

where

$$\left.\begin{aligned} U^{n}_{i+1/2,j} &= [u^{n}_{i+1/2,j,1},\ldots,u^{n}_{i+1/2,j,K}]^T, \quad V^{n}_{i,j+1/2} = [v^{n}_{i,j+1/2,1},\ldots,v^{n}_{i,j+1/2,K}]^T,\\ G^{n}_{i+1/2,j} &= h^{n}_{i+1/2,j}\Delta\sigma^T[\mathrm{F}u^{n}_{i+1/2,j,1} - \gamma_{i+1/2,j},\ldots,\mathrm{F}u^{n}_{i+1/2,j,K} - \gamma_{i+1/2,j}]^T,\\ G^{n}_{i,j+1/2} &= h^{n}_{i,j+1/2}\Delta\sigma^T[\mathrm{F}v^{n}_{i,j+1/2,1} - \gamma_{i,j+1/2},\ldots,\mathrm{F}v^{n}_{i,j+1/2,K} - \gamma_{i,j+1/2}]^T, \end{aligned}\right\} \tag{11}$$

with

$$\left.\begin{aligned} \gamma_{i+1/2,j} = (1-\theta)g\frac{\delta t}{\delta x}(\eta^{n}_{i+1,j} - \eta^{n}_{i,j}), \quad \gamma_{i,j+1/2} &= (1-\theta)g\frac{\delta t}{\delta y}(\eta^{n}_{i,j+1} - \eta^{n}_{i,j}),\\ \Delta\sigma &= \left[\delta\sigma'\frac{\partial\sigma}{\partial\sigma'}_1,\ldots,\delta\sigma'\frac{\partial\sigma}{\partial\sigma'}_K\right]^T. \end{aligned}\right\} \tag{12}$$

Note that $k = 1/2$ corresponds to the bed and $k = K + 1/2$ to the surface in this notation. The tridiagonal matrix $\boldsymbol{A}$ has different forms for the x- and y-directions although omitting the subcripts $(i+1/2, j)$ and $(i, j+1/2)$ the elements a_{lk} are defined in both cases by:

for $k = 1$,

$$a_{11} = h\delta\sigma'\frac{\partial\sigma}{\partial\sigma'}_1 + \delta t\frac{\nu(\mathrm{d}\sigma'/\mathrm{d}\sigma)_{1\frac{1}{2}}}{h\delta\sigma'} + \left(1 + \frac{\sigma_1 - \sigma_{1/2}}{\sigma_{1/2} - \sigma_0}\right)\delta t\frac{\nu(\mathrm{d}\sigma'/\mathrm{d}\sigma)_{1/2}}{h\delta\sigma'}$$

since the velocity just below the bed (at σ_0) is set to make the bed velocity zero assuming linear interpolation, and

$$a_{12} = -\delta t\frac{\nu(\mathrm{d}\sigma'/\mathrm{d}\sigma)_{1\frac{1}{2}}}{h\delta\sigma'};$$

for $k = 2,\ldots,K-1$,

$$a_{k,k-1} = -\delta t\frac{\nu(\mathrm{d}\sigma'/\mathrm{d}\sigma)_{k-1/2}}{h\delta\sigma'},$$

$$a_{k,k} = h\delta\sigma'\frac{\partial\sigma}{\partial\sigma'}_k + \delta t\frac{\nu(\mathrm{d}\sigma'/\mathrm{d}\sigma)_{k+1/2}}{h\delta\sigma'} + \delta t\frac{\nu(\mathrm{d}\sigma'/\mathrm{d}\sigma)_{k-1/2}}{h\delta\sigma'},$$

$$a_{k,k+1} = -\delta t\frac{\nu(\mathrm{d}\sigma'/\mathrm{d}\sigma)_{k+1/2}}{h\delta\sigma'};$$

and for $k = K$,

$$a_{K,K-1} = -\delta t \frac{\nu(\mathrm{d}\sigma'/\mathrm{d}\sigma)_{K-1/2}}{h\delta\sigma'}, \quad a_{K,K} = h\delta\sigma'(\partial\sigma/\partial\sigma')_K + \delta t \frac{\nu(\mathrm{d}\sigma'/\mathrm{d}\sigma)_{K-1/2}}{h\delta\sigma'}. \tag{13}$$

Substituting into the depth-integrated continuity equation gives

$$\eta_{i,j}^{n+1} = \beta_{i,j}^n - \theta\frac{\delta t}{\delta x}(h_{i+1/2,j}^n \Delta\sigma^T U_{i+1/2,j}^{n+1} - h_{i-1/2,j}^n \Delta\sigma^T U_{i-1/2,j}^{n+1}) - \theta\frac{\delta t}{\delta y}(h_{i,j+1/2}^n \Delta\sigma^T V_{i,j+1/2}^{n+1} - h_{i,j-1/2}^n \Delta\sigma^T V_{i,j-1/2}^{n+1}), \tag{14}$$

where

$$\beta_{i,j}^n = \eta_{i,j}^n - (1-\theta)\frac{\delta t}{\delta x}(h_{i+1/2,j}^n \Delta\sigma^T U_{i+1/2,j}^n - h_{i-1/2,j}^n \Delta\sigma^T U_{i-1/2,j}^n) - (1-\theta)\frac{\delta t}{\delta y}(h_{i,j+1/2}^n \Delta\sigma^T V_{i,j+1/2}^n - h_{i,j-1/2}^n \Delta\sigma^T V_{i,j-1/2}^n). \tag{15}$$

Substituting for U^{n+1} and V^{n+1} gives

$$\begin{aligned}
&\eta_{i,j}^{n+1} - \theta^2 g\frac{\delta t^2}{\delta x^2}[(h_{i+1/2,j}^n)^2 \Delta\sigma^T A_{i+1/2,j}^{-1}\Delta\sigma(\eta_{i+1,j}^{n+1} - \eta_{i,j}^{n+1}) - (h_{i-1/2,j}^n)^2 \Delta\sigma^T A_{i-1/2,j}^{-1} \\
&\quad \times\Delta\sigma(\eta_{i,j}^{n+1} - \eta_{i-1,j}^{n+1})] - \theta^2 g\frac{\delta t^2}{\delta y^2}[(h_{i,j+1/2}^n)^2 \Delta\sigma^T A_{i,j+1/2}^{-1}\Delta\sigma(\eta_{i,j+1}^{n+1} - \eta_{i,j}^{n+1}) \\
&\quad -(h_{i,j-1/2}^n)^2 \Delta\sigma^T A_{i,j-1/2}^{-1}\Delta\sigma(\eta_{i,j}^{n+1} - \eta_{i,j-1}^{n+1})] \\
&= \beta_{i,j}^n - \theta\frac{\delta t}{\delta x}[h_{i+1/2,j}^n(\Delta\sigma^T A_{i+1/2,j}^{-1} G_{i+1/2,j})^n - h_{i-1/2,j}^n(\Delta\sigma^T A_{i-1/2,j}^{-1} G_{i-1/2,j})^n] \\
&\quad -\theta\frac{\delta t}{\delta y}[h_{i,j+1/2}^n(\Delta\sigma^T A_{i,j+1/2}^{-1} G_{i,j+1/2})^n - h_{i,j-1/2}^n(\Delta\sigma^T A_{i,j-1/2}^{-1} G_{i,j-1/2})^n].
\end{aligned} \tag{16}$$

Here $\Delta\sigma^T A^{-1}\Delta\sigma$ is a positive number. For each point i, j we thus have an equation for $\eta_{i,j}, \eta_{i+1,j}, \eta_{i,j+1}, \eta_{i-1,j}, \eta_{i,j-1}$ giving a five-diagonal equation set. The resulting $I \times J$ equations are solved efficiently using a conjugate gradient solver. Having solved for η the velocities u and v are obtained by solving the tridiagonal equations (9) and (10). The vertical velocity ω at the new time level $n+1$ may now be simply determined from equation (2) as

$$\omega_{i,j,k+1/2}^{n+1} = \omega_{i,j,k-1/2}^{n+1} - \delta\sigma'\frac{\partial\sigma}{\partial\sigma'}_k\left(\frac{\eta_{i,j}^{n+1} - \eta_{i,j}^n}{\delta t} + \frac{h_{i+1/2,j}^{n+1}u_{i+1/2,j,k}^{n+1} - h_{i-1/2,j}^{n+1}u_{i-1/2,j,k}^{n+1}}{\delta x} + \frac{h_{i,j+1/2}^{n+1}v_{i,j+1/2,k}^{n+1} - h_{i,j-1/2}^{n+1}v_{i,j-1/2,k}^{n+1}}{\delta y}\right). \tag{17}$$

The vertical velocity in physical space w may also be obtained from a finite-difference form of equation (5) when needed.

We now define the explicit operators $\mathrm{F}u$ and $\mathrm{F}v$ which are second-order accurate in time for advection and horizontal diffusion according to the Adams–Bashforth scheme. Starting with the advective components $\mathrm{F}u^a, \mathrm{F}v^a$ we define operators $\mathrm{f}u^a, \mathrm{f}v^a$ for a given time level so that

$$\mathrm{F}u^a = (3(\mathrm{f}u^a)^n - (\mathrm{f}u^a)^{n-1})/2, \tag{18}$$

with a similar expression for $\mathrm{F}v^a$. To demonstrate the procedure figure 3 shows a cell

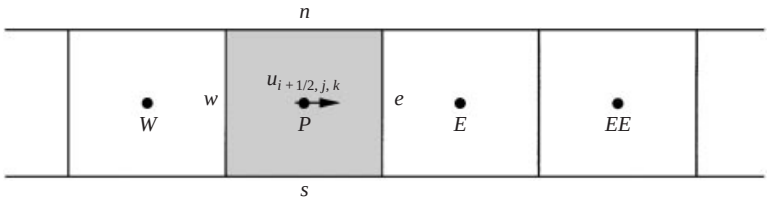

FIGURE 3. Advection scheme.

centred on $u_{i+1/2,j,k}$ and for the transport quantity ϕ (hu in equation (3)). $\mathrm{f}u^a$ is thus given by

$$\mathrm{f}u^a_{i+1/2,j,k} = -\frac{\delta t}{h_{i+1/2,j}}\left(\frac{u_e\phi_e - u_w\phi_w}{\delta x} + \frac{v_n\phi_n - v_s\phi_s}{\delta y} + \frac{\omega_u u_u - \omega_d u_d}{\delta\sigma'(\partial\sigma/\partial\sigma')_P}\right) \tag{19}$$

where $u_e, u_w, v_n, v_s, \omega_u, \omega_d$ are obtained by linear interpolation, e.g.

$$u_e = (u_{i+1/2,j,k} + u_{i+1\frac{1}{2},j,k})/2,$$
$$v_n = (v_{i,j+1/2,k} + v_{i+1,j+1/2,k})/2,$$
$$\omega_u = (\omega_{i,j,k+1/2} + \omega_{i+1,j,k+1/2})/2,$$

and $\phi_e, \phi_w, \phi_n, \phi_s, \phi_u, \phi_d$ are obtained from an upwind interpolation scheme. Here we use the QUICK scheme which is found to be sufficiently stable for this application and is second-order accurate. This gives for ϕ_e for example

$$\text{for } u_e > 0: \quad \phi_e = (3\phi_E + 6\phi_P - \phi_W)/8,$$
$$\text{for } u_e \leqslant 0: \quad \phi_e = (3\phi_P + 6\phi_E - \phi_{EE})/8.$$

Note also that, to determine $\phi = uh$, h is also given by linear interpolation.

There is a corresponding scheme for $\mathrm{F}v^a$ with $\phi = hv$ in equation (4).

The explicit components of $\mathrm{F}u, \mathrm{F}v$ due to horizontal diffusion $\mathrm{F}u^{hd}, \mathrm{F}v^{hd}$ are second-order in time according to the Adams–Bashforth scheme and are defined by $\mathrm{f}u^{hd}, \mathrm{f}v^{hd}$ for a given time level as in equation (18). $\mathrm{f}u^{hd}, \mathrm{f}v^{hd}$ require horizontal gradients in real space due to errors in σ-coordinates identified by Haney (1991) and the method of calculation involving interpolation along vertical lines is identical to that in Stansby (1997).

The specification of $\mathrm{F}u_{i+1/2,j,k}$ is now completed with terms, $u\,\partial h/\partial t$ and $w_g\,\partial u/\partial\sigma$ in equations (3) and (4), omitting subscripts $i+1/2, j$ for conciseness, as

$$\mathrm{F}u_k = u_k + \mathrm{F}u^a_k + \mathrm{F}u^{hd}_k - u_k\frac{(h^n - h^{n-1})}{\delta t} + w_{g_k}\frac{\partial\sigma'}{\partial\sigma_k}\frac{(u^n_{k+1} - u^n_{k-1})}{2\delta\sigma'},$$

and of $\mathrm{F}v_{i,j+1/2,k}$ with terms, $v\,\partial h/\partial t$ and $w_g\,\partial v/\partial\sigma$, omitting subscripts $i, j+1/2$, as

$$\mathrm{F}v_k = v_k + \mathrm{F}v^a_k + \mathrm{F}v^{hd}_k - v_k\frac{(h^n - h^{n-1})}{\delta t} + w_{g_k}\frac{\partial\sigma'}{\partial\sigma_k}\frac{(v^n_{k+1} - v^n_{k-1})}{2\delta\sigma'},$$

where, again omitting the horizontal subscripts,

$$w_{g_k} = \frac{\sigma_k(h^n - h^{n-1}) + (\eta^n - \eta^{n-1})}{\delta t}.$$

The numerical scheme is thus complete apart from consideration of boundary conditions and wetting and drying which are described below.

4. Boundary conditions

Inlet and outlet boundary conditions for subcritical flow are conventionally specified by either surface elevation at outflow and velocity flux at inflow or vice versa. In this application there are however some additional complications which are considered below.

Wetting or drying as a water surface moves up or down a slope is handled simply. All surface elevations are advanced as part of the general solution and dry cell columns have zero velocity on their cell faces. In this context a 'cell column' refers to a cell in the horizontal plane and all its vertical cells. If the depth in a wet cell column decreases below a small specified value ϵ then the cell column becomes dry. If the depth in a dry cell column increases above ϵ, the surface elevation is given the value equal to that of the nearest wet cell column most nearly normal to the wet/dry boundary line; the velocities on the cell faces remain zero and the cell column is effectively passive before being advanced normally at the next time step. In this way, once a newly wet cell column has been flagged, its surface elevation is then defined from information in the neighbouring wet domain. This is physically realistic and numerically stable provided the time step is small enough for the wet/dry boundary to advance/recede by no more than one (horizontal) cell in a time step.

The inflow/outflow conditions are required to reproduce the near-surface velocities measured in the laboratory flume. Without the island in position the flow was found to be almost uniform over at least the central 75% of the flume length. However, simply imposing corresponding velocity fluxes based on near-surface velocity at inflow and outflow with an appropriate surface elevation variation at one end resulted in velocities about 60% too high over most of the flow. It should be mentioned that the flow rates discharging into and out of the flume were not measured in the experiment. This magnification is obviously partly due to the fact that velocity flux input should be based on the depth-averaged, not surface, velocity and partly due to seiching superimposed on the 'forced' oscillation. To obtain the background surface velocities of the experiment in the computational model the inflow/outflow conditions were corrected by a simple feedback method with velocity flux specified at one end and surface elevation variation only at the other. The input velocity flux is simply reduced, to $c_1\times$ that defined by surface velocity in the experiment, where c_1 is between 0.62 and 0.81 and each case has to be tuned through numerical experiment. The surface elevation variation is determined by assuming $\partial\eta/\partial t = -(1/gh)\partial q/\partial t$ where flux $q = uh$. The surface elevation on the boundary cell columns is thus adjusted at the end of each time step using an appropriate value of q. This is determined by calculating the actual flux q_a close to boundary (at a distance of 1/8th of the flume length from the end generally). We then set $q = c_2(q_r - (q_a - q_r))$ where q_r is the required value and c_2 is a factor determined from numerical experiment, between 0.56 and 0.74 for these cases. c_1 and c_2 are listed in table 1 for each case investigated, together with details of the test conditions. The velocities in the central 75% of the flume were uniform to within 4% with a maximum at the centre. Since the island wakes are generated and evolve in a much smaller region the background flow may be considered to be very close to uniform. While this is clearly a pragmatic approach to reproducing experimental conditions the two tuning parameters required little adjustment and the required results could be obtained after three or four attempts. It should be mentioned that while the tuning was undertaken without the island in position the velocities near the end boundaries were rechecked with the island in position, as its resistance may affect the seiching, but further adjustment was not found necessary.

Run name	T (s)	U_0 ($\mathrm{m\,s^{-1}}$)	h (m)	D (m)	KC	β	a (m)	Re_a ($\times 10^4$)	c_f ($\times 10^{-3}$)	S	Fr	c_1	c_2
CI02	60	0.035	0.046	0.42	5.0	2954	0.33	1.17	18.5	0.17	0.05	0.66	0.6
CI05	70	0.092	0.046	0.42	15.3	2532	1.02	8.26	6.96	0.06	0.14	0.77	0.7
CI07	120	0.043	0.032	0.52	9.9	2262	0.82	3.53	10.6	0.17	0.08	0.81	0.74
CI08	80	0.030	0.026	0.56	4.3	3976	0.38	1.15	18.7	0.40	0.05	0.62	0.56
CI17	190	0.050	0.018	0.62	15.3	2030	1.51	7.56	7.27	0.25	0.12	0.68	0.62

TABLE 1.

5. Results

Velocity vector/vorticity plots corresponding to five cases investigated experimentally (as listed in table 1) are presented in figures 4–8, corresponding to the full range of wake structures from symmetric without vortex pairing to complex vortex shedding. The horizontal computational domain was 9.8 m × 3.3 m and horizontal grids of 178 × 60 and 356 × 120 were used. Fifteen vertical cells were generally used with the bed cell size set approximately equal to $\sqrt{2\nu\delta t}$. The grid points on the coarser mesh are at the same spacing as those on which the velocities are interpolated from the PTV in the experiments so that vorticity structures of the same resolution may be compared for the model and experiment. The fine mesh has a spacing of half that of the coarse mesh and vorticity of the same resolution on the fine mesh may be obtained from velocities at every other mesh point. The vorticity structures of this resolution on the fine mesh and the coarse mesh were very similar (in all but one case mentioned below), showing that the numerical scheme had converged to within the resolution obtained experimentally. However using the fine computational mesh to define vorticity showed smaller-scale structures than on the coarse mesh and the computational scheme had thus not converged in this sense.

Results for surface conditions are shown to compare directly with experiment. Figure 4 shows results for $KC = 4.3$ and $S = 0.40$ (run CI08 in table 1), referred to as symmetric without pairing in Part 1, at $t/T = 0.25$, 0.5, 0.625, 0.75. While there is general agreement between computation and experiment, the experiment is less symmetric and in the computation there is some evidence of weak pairing with vorticity created in a previous half-cycle.

Figure 5 shows results for $KC = 15.5$ and $S = 0.25$ (run CI17) at the same times as above, giving wakes referred as symmetric with pairing. Here there is close agreement between experiment and computation with the experiment remaining more symmetric than in the previous case.

Figure 6 shows results for $KC = 9.9$ and $S = 0.17$ (run CI07) called sinuous with pairing. The general wake structures are similar in the experiment and computation although the details in relation to vortex pairing can be different at certain times, e.g. $t/T = 0.625$, and very similar before and after, at $t/T = 0.25$ and 0.75.

Figure 7 shows the vortex shedding wake phenomenon for $KC = 5.0$ and $S = 0.17$ (run CI02). These results were produced with the finer mesh; in this case the coarser mesh produced more symmetric wake formation. The general features are reproduced in the computation with one substantial vortex region shed per half-cycle with vorticity crossing from one side of the island to the other in a half-cycle. This is a distinguishing feature of vortex shedding flows compared with symmetric or sinuous vortex pairing flows described above. Details can however be quite different, notably at $t/T = 0.625$

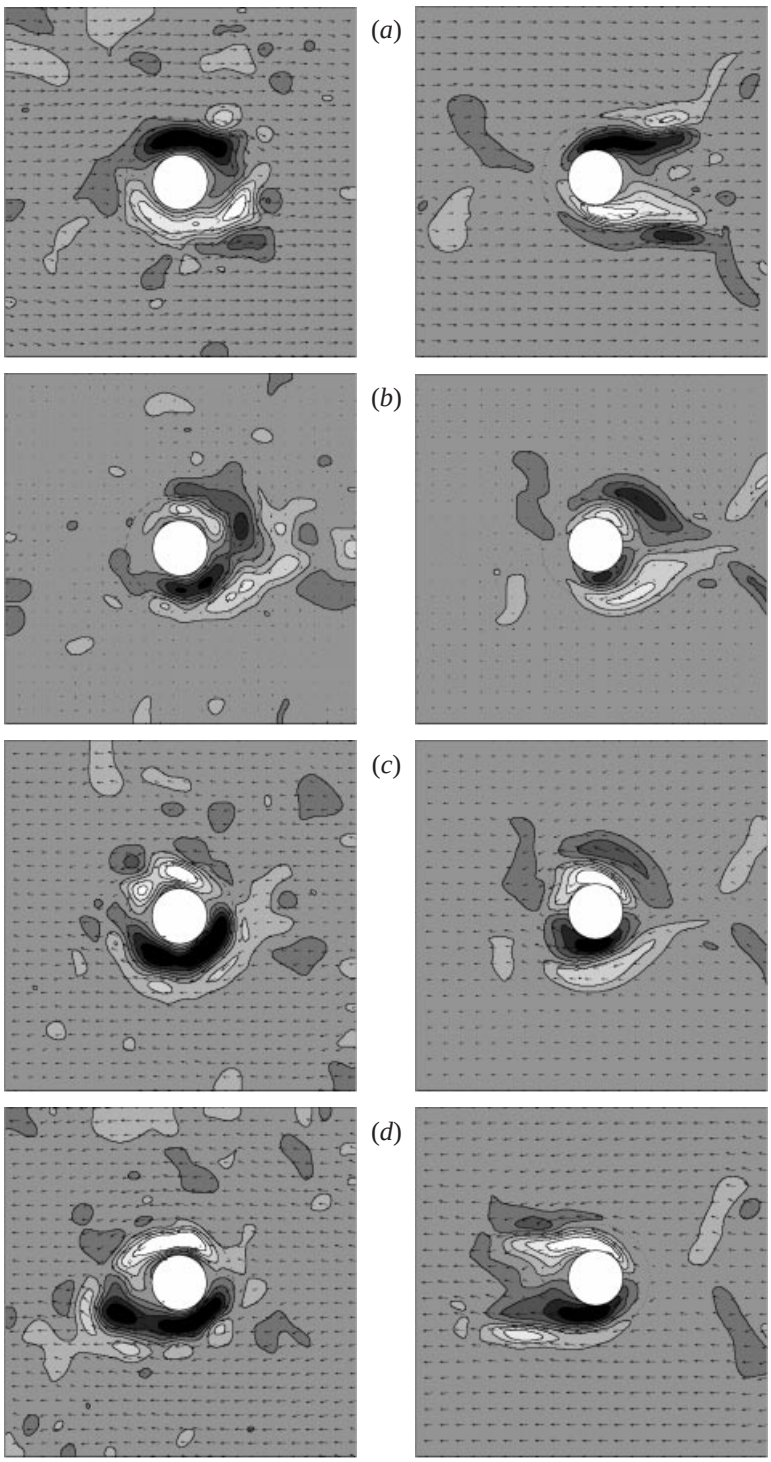

FIGURE 4. Surface velocities and vorticity for $KC = 4.3, S = 0.40$ and $D/h = 21.7$ (run CI08) for experiment (left) and model (right). (*a*) $t/T = 0.25$, (*b*) $t/T = 0.5$, (*c*) $t/T = 0.625$, (*d*) $t/T = 0.75$.

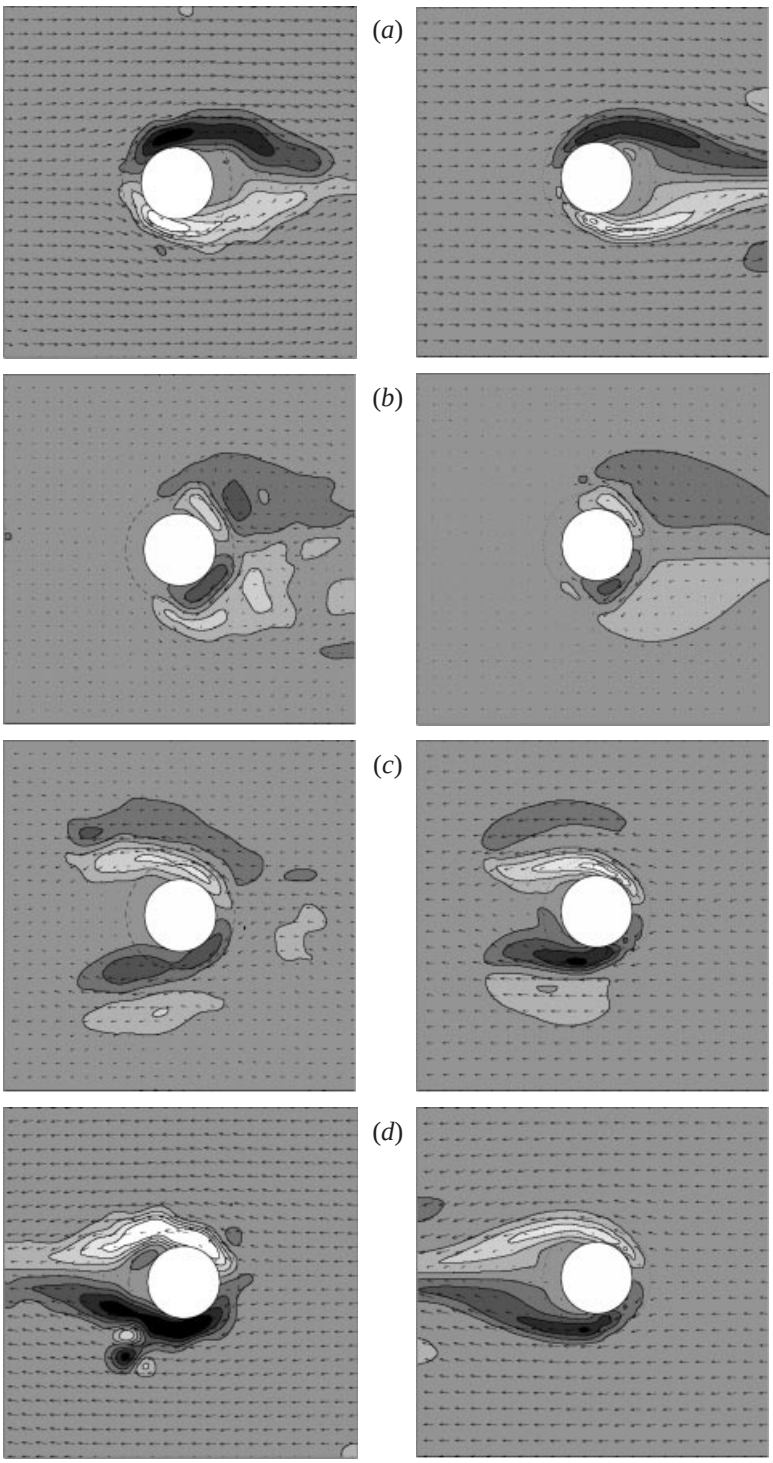

FIGURE 5. Surface velocities and vorticity for $KC = 15.5, S = 0.25$ and $D/h = 34.5$ (run CI17) for experiment (left) and model (right) (*a*) $t/T = 0.25$, (*b*) $t/T = 0.5$, (*c*) $t/T = 0.625$, (*d*) $t/T = 0.75$.

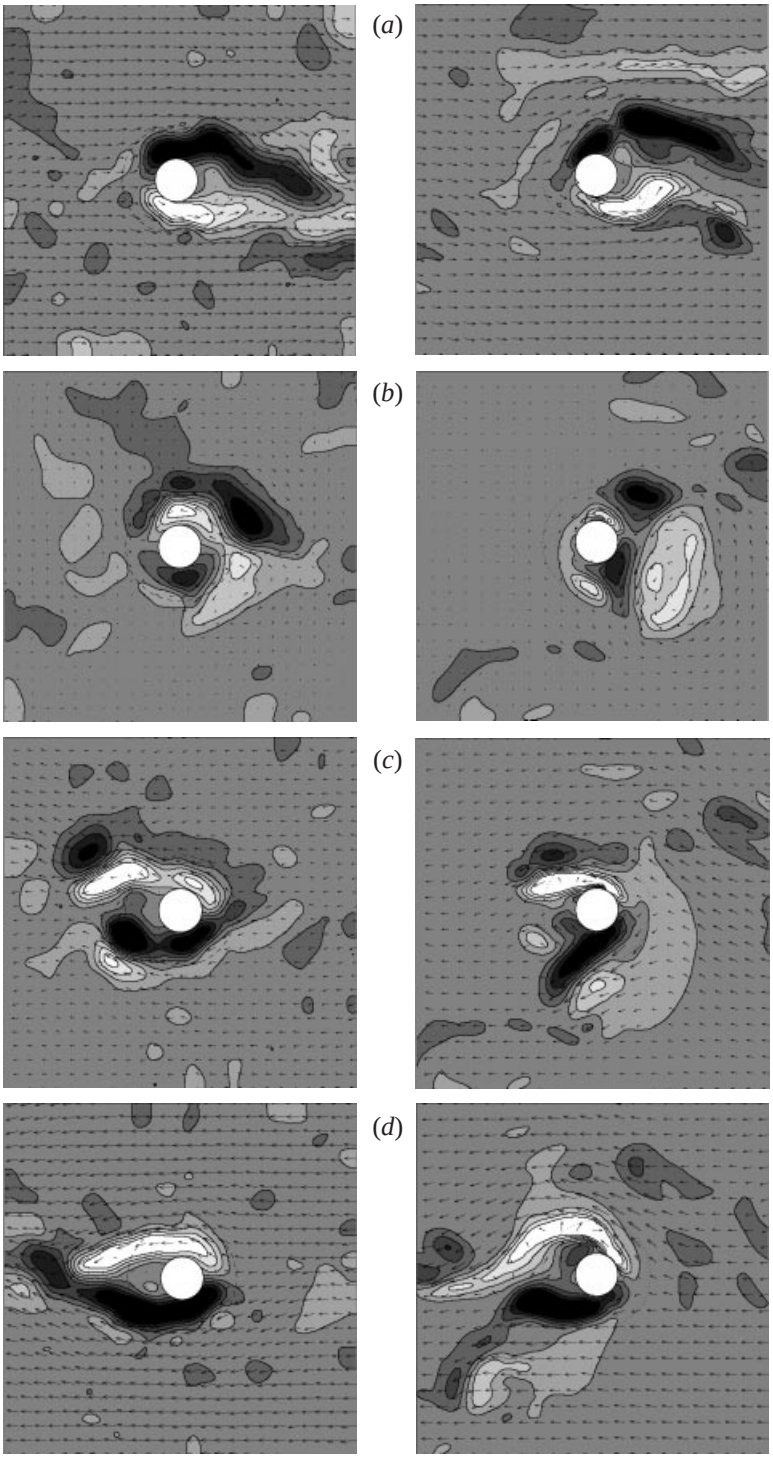

FIGURE 6. Surface velocities and vorticity for $KC = 9.9, S = 0.17$ and $D/h = 16.3$ (run CI07) for experiment (left) and model (right). (*a*) $t/T = 0.25$, (*b*) $t/T = 0.5$, (*c*) $t/T = 0.625$, (*d*) $t/T = 0.75$.

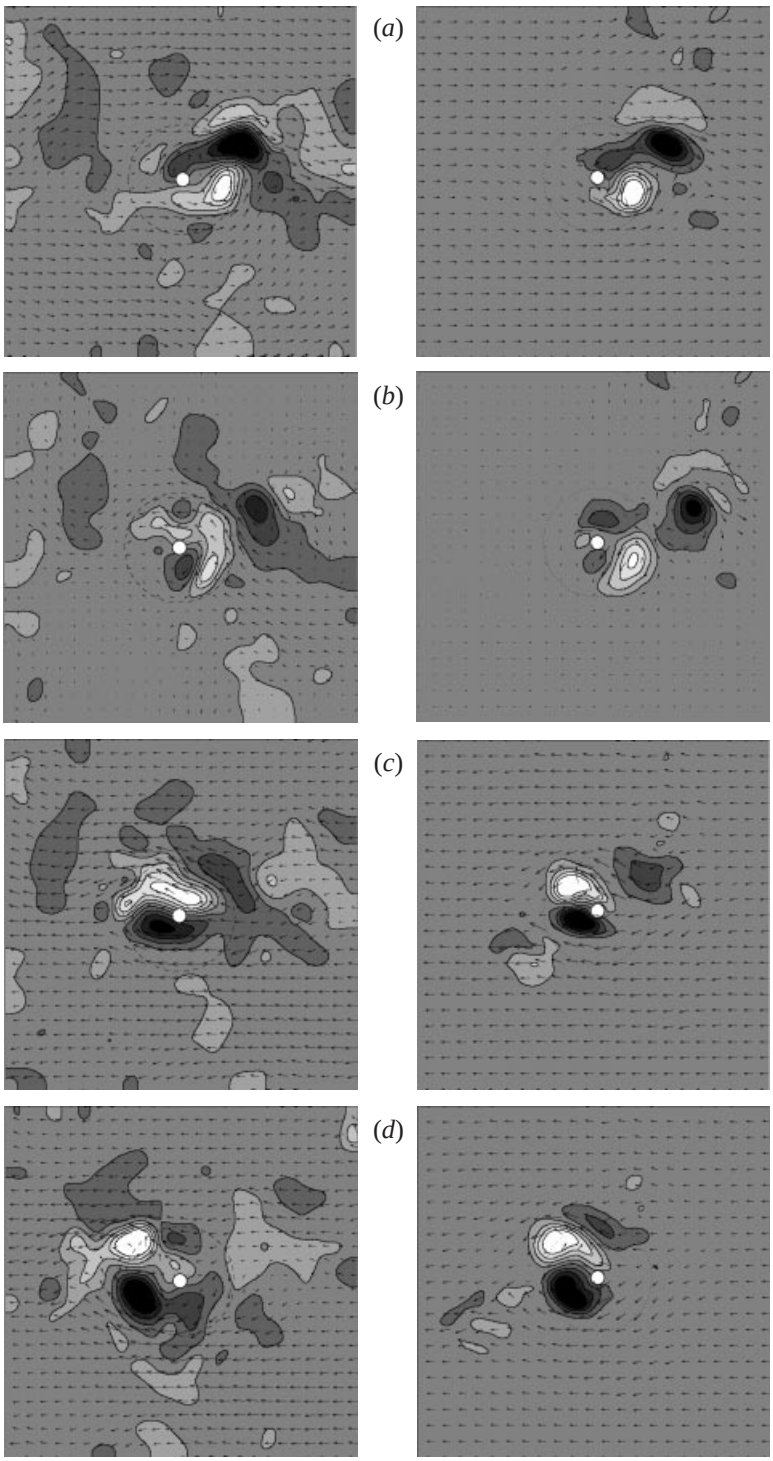

FIGURE 7. Surface velocities and vorticity for $KC = 5.0, S = 0.17$ and $D/h = 9.2$ (run CI02) for experiment (left) and model (right). (*a*) $t/T = 0.25$, (*b*) $t/T = 0.5$, (*c*) $t/T = 0.625$, (*d*) $t/T = 0.75$.

with regard to the size of the vorticity regions. Although this case is less stable than the previous one, the KC value is lower and the S value is the same indicating the effect of different D/h values mentioned in Part 1.

A more complex vortex shedding flow with $KC = 15.3$ and $S = 0.063$ (run CI05) is shown in figure 8; in this case the depth-averaged velocities and vorticity structures are shown as well as the surface values and can be seen to be very similar despite the wake complexity. Here the double-pair structure in each half-cycle is broadly reproduced in the computations, although flow details can again be quite dissimilar. For example at $t/T = 0.625$ the weak anti-clockwise vorticity below the island in the experiment is not present in the computation and at $t/T = 0.75$ the anti-clockwise vorticity above the cylinder has been divided into two in the experiment while remaining as one coherent area in the computation. However it should be stressed that, for this case and the previous vortex shedding case, the wake is rather complex and not perfectly repetitive so it is perhaps only to be expected that the general flow features are reproduced.

6. Discussion and conclusions

It has been demonstrated that a shallow-water, boundary-layer solution is capable of reproducing the general features of a range of complex wake flows observed experimentally for oscillatory flows around conical islands of small slope. It should be stressed that the numerical predictions here are at the same resolution as the experiments for direct comparison and numerical convergence at this resolution is usually demonstrated. This is different from numerical convergence in the absolute sense that fine-scale flow features become independent of reducing mesh size and this was not achieved with the mesh sizes used here. It would of course be interesting to improve the resolution in the experiments and computations; however this is far from straightforward experimentally.

The intention when setting up the experiments was that they should be at low Froude numbers and indeed the maximum ambient value is 0.15. However the local Froude number is likely to increase as depth decreases close to the island and at the wet/dry interface it has uncertain behaviour which is probably not significant as velocities are very small. In the computations local Froude numbers, based on depth-averaged velocity magnitude, were maximum close to, but not at, the wet/dry intersection in regions where the velocity due to a vortex was reinforced by the onset flow velocity. In very local regions Froude number could be as high as unity although generally it was well below 0.5. It is uncertain whether Froude number can ever be sufficiently low to be insignificant, but there was little evidence of other than very local wave formation in the experiments or computations (which should pick this up with the numerical scheme used). Froude number is thus thought not to be a significant effect but a detailed study of when it does become significant would be valuable.

The velocity variation over the vertical is also of great interest. This was not intended to be a subject of this investigation as detailed experimental measurements are not yet available for comparison. However some preliminary computational results for near-bed and surface velocities showed that, well away from the wake regions, near-bed velocity generally lagged surface velocity as might be expected. However in the wake regions, in the lee of the island, the situations are clearly complex with substantial periods when the near-bed velocity is in the opposite direction to the

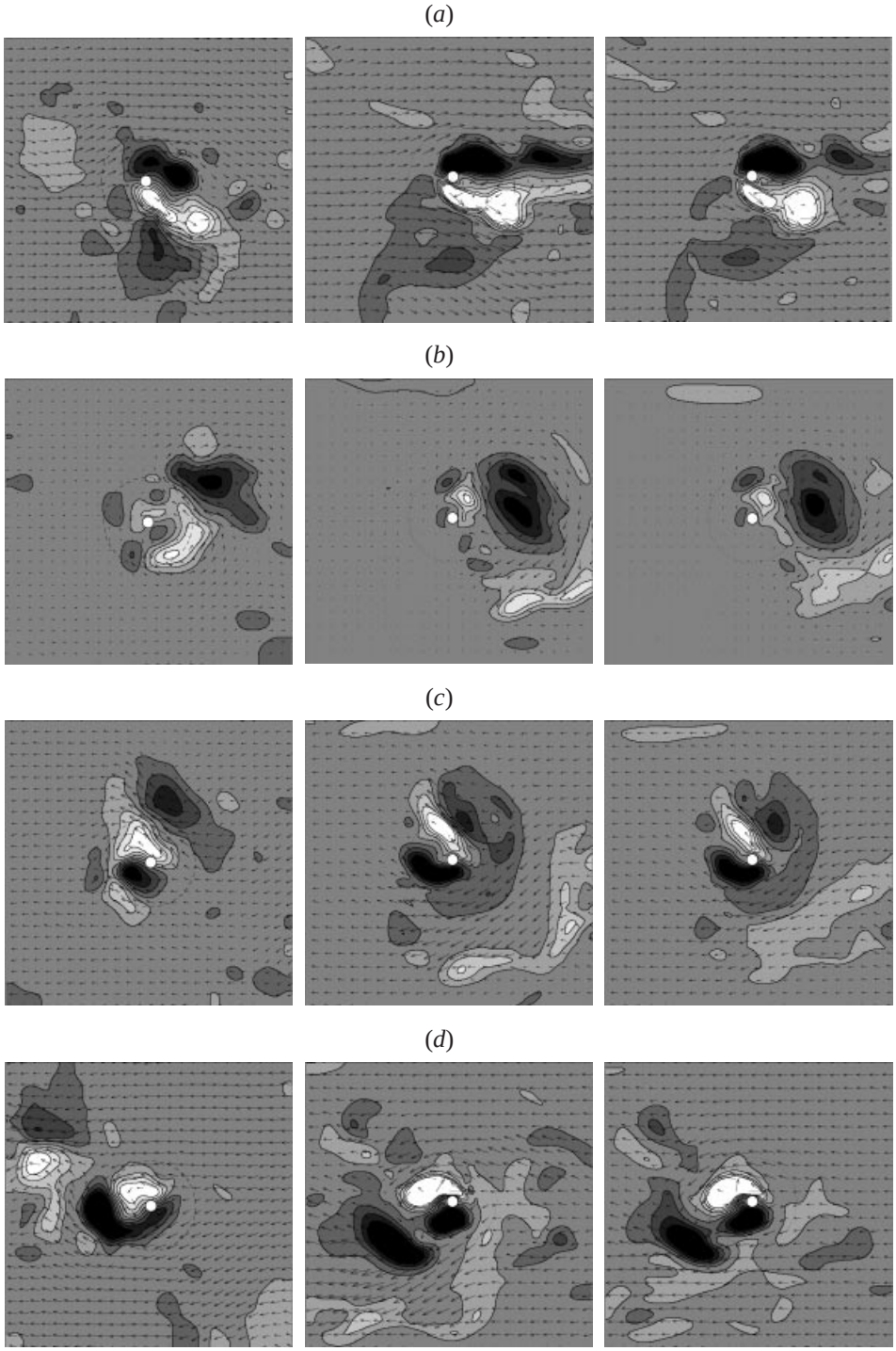

FIGURE 8. Surface velocities and vorticity for $KC = 15.3, S = 0.063$ and $D/h = 9.2$ (run CI05) for experiment (left) and model (centre), including depth-averaged values for the model (right). (*a*) $t/T = 0.25$, (*b*) $t/T = 0.5$, (*c*) $t/T = 0.625$, (*d*) $t/T = 0.75$.

surface velocity, although depth-averaged and surface vorticities (and velocities) are similar as shown in figure 8.

With regard to numerical modelling, the boundary-layer, shallow-water approach is a practical computing proposition on a modern PC with run times of order one day for these problems. Inclusion of non-hydrostatic pressure increases run time markedly but will become more important as slope increases, particularly close to the obstacle where separation in a vertical plane may occur. Some two-dimensional vertical plane problems have been assessed (Stansby & Zhou 1998), indicating that non-hydrostatic effects become noticeable for slopes greater than about 10°.

While this paper demonstrates the capability of shallow-water, boundary-layer modelling for laminar flows, turbulence modelling is necessary for engineering or environmental problems. Modelling of linear oscillatory flows by the k–ϵ eddy-viscosity approach gives accurate bed shear stresses and eddy viscosities generally within experimental error (Letherman *et al.* 2000). However in more general shallow-water flows appropriate horizontal turbulence modelling strategies need to be determined.

Support through EPSRC grants GR/K/76481 and GR/K/95666 is gratefully acknowledged.

REFERENCES

Casulli, V. 1990 Semi-implicit finite-difference methods for the two-dimensional shallow-water equations. *J. Comput. Phys.* **86**, 56–74.

Casulli, V. & Cattani, E. 1994 Stability, accuracy and efficiency of a semi-implicit method for three-dimensional shallow-water flow. *Comput. Math. Applics.* **27**, 99–112.

Haney, R. L. 1991 On the pressure gradient force over steep topography in σ coordinate ocean models. *J. Phys. Oceanogr.* **21**, 610–619.

Leendertse, J. J. 1967 Aspects of a computational model for long period wave propagation. *Memo* RM-5294-PR. Rand Corp., Santa Monica, CA.

Letherman, S. A., Cotton, M. A., Stansby, P. K., Chen, C. & Chen. D. 2000 Turbulence model predictions for oscillatory rough-bed oscillatory flows. *J. Hydroinformatics* (to appear).

Lloyd, P. M., Stansby, P. K. & Chen, D. 2001 Wake formation around islands in oscillatory laminar shallow-water flows. Part 1. Experimental investigation. *J. Fluid Mech.* **429**, 217–238.

Phillips, N. A. 1957 A coordinate system having some special advantages for numerical forecasting. *J. Met.* **14**, 184–185.

Stansby, P. K. 1997 Semi-implicit finite-volume shallow-water flow and transport solver. *Intl J. Numer. Meth. Fluids* **25**, 285–313.

Stansby, P. K. & Zhou, J. G. 1998 Shallow-water flow solver with non-hydrostatic pressure: 2D vertical plane problems. *Intl J. Numer. Meth. Fluids* **28**, 541–563.

Zhou, J. G. & Stansby, P. K. 1999 An arbitrary Lagrangian–Eulerian σ (ALES) model with non-hydrostatic pressure for shallow-water flows. *Comput. Meth. Appl. Mech. Engng* **178**, 199–214.